J. Fluid Mech. (2024), *vol*. 1001, A58, doi:10.1017/jfm.2024.1158

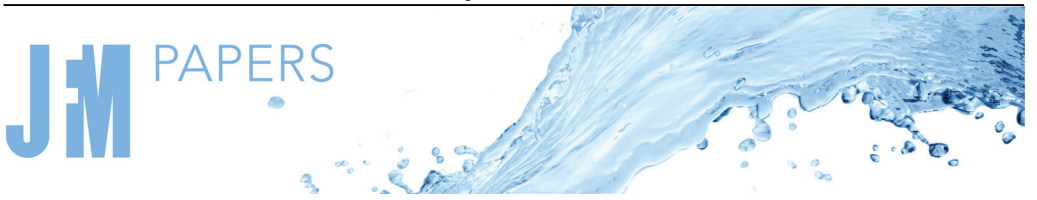

Capillary lubrication of a spherical particle near a fluid interface

Aditya Jha[1], **Yacine Amarouchene**[1] **and Thomas Salez**[1],†

[1]University of Bordeaux, CNRS, LOMA, UMR 5798, F-33405 Talence, France

(Received 22 July 2024; revised 2 December 2024; accepted 2 December 2024)

The lubricated motion of an object near a deformable boundary presents striking subtleties arising from the coupling between the elasticity of the boundary and lubricated flow, including but not limited to the emergence of a lift force acting on the object despite the zero Reynolds number. In this study, we characterize the hydrodynamic forces and torques felt by a sphere translating in close proximity to a fluid interface, separating the viscous medium of the sphere's motion from an infinitely more viscous medium. We employ lubrication theory and perform a perturbation analysis in capillary compliance. The dominant response of the interface owing to surface tension results in a long-ranged interface deformation, which leads to a modification of the forces and torques with respect to the rigid reference case, that we characterize in detail with scaling arguments and numerical integrations.

Key words: capillary flows, lubrication theory, microscale transport

1. Introduction

The dynamics of objects moving in viscous fluids has been studied both theoretically and experimentally for a long time (Jeffery 1915; Lamb 1924; Collins 1955; Dean & O'Neill 1963; O'Neill 1964; Batchelor 1967). Confining the viscous flow between an object and a rigid surface modifies the forces felt by the object (Goldman, Cox & Brenner 1967; O'Neill & Stewartson 1967; Cooley & O'Neill 1969; Jeffrey & Onishi 1981). Such a modification is involved in vastly different phenomena ranging from the mechanics of joints (Hou *et al.* 1992; Hlaváček 1993), to the movement of cells in capillaries (Abkarian, Lartigue & Viallat 2002) and the dynamics of suspensions (Batchelor 1970, 1971, 1976, 1977; Happel & Brenner 1983).

Recent research has provided evidence of boundary elasticity further modifying the lubricated dynamics of an object (Leroy & Charlaix 2011; Leroy *et al.* 2012). Further standardization of the measurement process has led to the design of contactless probes

† Email address for correspondence: thomas.salez@cnrs.fr

for rheology (Garcia *et al.* 2016; Basoli *et al.* 2018). The coupling of boundary elasticity and lubrication flow, collectively termed soft lubrication, predicts the emergence of lift forces exerted on particles translating parallel to soft boundaries (Sekimoto & Leibler 1993; Beaucourt, Biben & Misbah 2004; Skotheim & Mahadevan 2005; Weekley, Waters & Jensen 2006; Urzay, Llewellyn Smith & Glover 2007; Snoeijer, Eggers & Venner 2013; Bouchet *et al.* 2015; Salez & Mahadevan 2015; Essink *et al.* 2021; Bertin *et al.* 2022; Bureau, Coupier & Salez 2023; Rallabandi 2024). Such lift forces are associated with the symmetry breaking arising out of the deformability. Since the latter is crucial to the generated force, the nature of the bounding wall has been further explored by examining the influence of slip (Rinehart *et al.* 2020), and viscoelasticity (Pandey *et al.* 2016; Kargar-Estahbanati & Rallabandi 2021). A reversal of the nature of the lift force from repulsive to attractive has also been predicted for viscoelastic settings (Hu, Meng & Doi 2023). Other studies have explored the complex modifications induced by including inertial effects (Clarke & Potnis 2011) and compressibility (Balmforth, Cawthorn & Craster 2010). On the experimental front, dedicated research has verified the presence of these lift forces on various substrates (Saintyves *et al.* 2016; Davies *et al.* 2018; Rallabandi *et al.* 2018; Vialar *et al.* 2019; Zhang *et al.* 2020).

In biology, where cells and tissues are extremely soft, and/or at small scales in soft matter, the interfacial capillary stress at the boundary dominates over bulk elasticity. By employing a classical Stokeslet-like response of the flow near a fluid interface, it has been shown that a rectified flow may be generated owing to the tension of the boundary (Aderogba & Blake 1978; Nezamipour & Najafi 2021). On the other hand, finite-size effects were addressed (Lee, Chadwick & Leal 1979; Lee & Leal 1980, 1982; Geller, Lee & Leal 1986) in the regime of a large gap between the object and the fluid interface, predicting counter-intuitive behaviours unique to capillarity. The results of these studies have been useful in analysing the movement of microorganisms near a fluid interface (Trouilloud *et al.* 2008; Lopez & Lauga 2014), as well as the formation of floating biofilms (Desai & Ardekani 2020). Recently, capillary-lubrication studies (Jha, Amarouchene & Salez 2023, 2024) have characterized the dynamics of an infinite cylinder near a fluid interface, highlighting the influence of the viscosity contrast and thickness ratio between the two fluid layers, and leading to large variability in the forces generated as opposed to elastic interfaces.

While previous research has highlighted the importance of understanding lubricated motion near a fluid interface, the characterization of the dynamics of a particle moving with multiple degrees of freedom near a fluid interface remains to be explored. In this article, we explore in detail the translational motion of a sphere moving in close proximity to an infinitely viscous but deformable sublayer. In the small-deformation limit, we calculate the forces and torques generated on the sphere during the motion. Due to a symmetry between translational and rotational motions in soft lubrication (Bertin *et al.* 2022), our work immediately generalizes to the case where rotation would be added. The remainder of the article is organized as follows. We start by describing the capillary-lubrication framework, before presenting the theoretical methodology for obtaining the different fields using perturbation analysis at small deformations of the fluid interface. We then discuss the implications of the interfacial deformation, and the competition between gravity and capillarity, on the forces and torques generated on the particle. Limiting expressions are derived for the capillary-dominated and gravity-dominated responses. While the former case is novel, the latter is reminiscent of a Winkler solid.

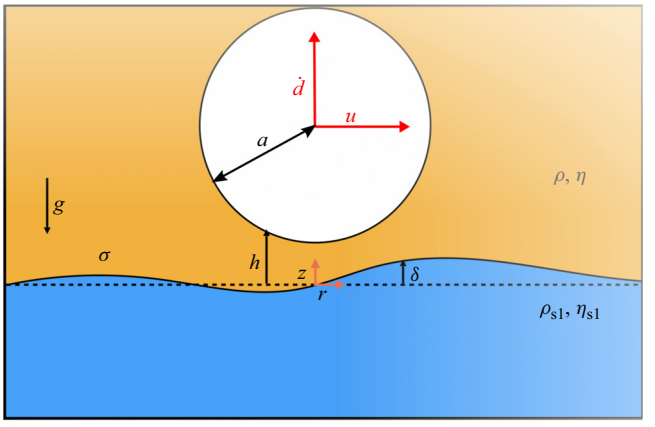

Figure 1. Schematic of the system. A sphere of radius a immersed in a viscous fluid of viscosity η and density ρ moves near a fluid interface. The undeformed gap profile is noted $h(r, t)$, with r the horizontal radial coordinate and t the time. The origin of coordinates is located at the undeformed fluid interface ($z = 0$) in line with the centre of mass of the sphere ($r = 0$). The interface separates the top fluid from a secondary fluid of viscosity η_{sl}, with $\eta_{sl} \gg \eta$, and density ρ_{sl} at the bottom, i.e. $\rho_{sl} > \rho$. The sphere has prescribed horizontal velocity u and vertical velocity $\dot{d}$, where $d = h(0, t)$ denotes the instantaneous distance between the sphere bottom and the undeformed fluid interface. The interface deflection field is denoted as $\delta(r, t)$, the acceleration due to gravity is denoted as g and the surface tension is denoted as σ.

2. Capillary-lubrication theory

We consider a sphere of radius a translating with a prescribed time-dependent horizontal velocity $\boldsymbol{u} = u(t)\boldsymbol{e}_x$ near a fluid interface, as shown in figure 1. The interface is characterized by its surface tension σ, and separates two incompressible Newtonian viscous liquids with dynamic shear viscosities η and η_{sl}, as well as densities ρ and ρ_{sl} (with $\rho < \rho_{sl}$). The acceleration due to gravity is denoted by g. The gap profile between the sphere and the undeformed fluid interface is denoted by $h(r, t)$, which depends on the horizontal radial coordinate r and time t. The x-direction oriented along $\boldsymbol{e}_x$ corresponds to the horizontal angular coordinate $\theta = 0$. The time-dependent distance between the bottom of the sphere's surface and the undeformed interface is denoted by $d(t)$, with $d > 0$. Its temporal derivative $\dot{d}(t)$ denotes the vertical velocity of the sphere. We focus on the case where the bottom layer is extremely viscous compared with the top layer, i.e. $\eta_{sl} \gg \eta$, and is infinitely thick compared with the gap between the sphere and the undeformed interface. These conditions allow us to assume that the tangential velocity at the fluid interface vanishes because the shear stress from the top layer is insufficient to generate a flow in the lower layer.

We neglect fluid inertia and assume that the typical gap between the sphere and the interface is much smaller than the typical horizontal length scale, allowing us to invoke lubrication theory (Reynolds 1886; Oron, Davis & Bankoff 1997). Introducing the excess pressure field p, in the top layer, with respect to the hydrostatic contribution, and the horizontal velocity field $\boldsymbol{v}$ of the fluid in the gap, the incompressible Stokes equations thus read at leading lubrication order

$$\frac{\partial p}{\partial z} = 0, \tag{2.1}$$

$$\boldsymbol{\nabla} p = \eta \frac{\partial^2 \boldsymbol{v}}{\partial z^2}, \tag{2.2}$$

where $\boldsymbol{\nabla}$ denotes the gradient in the horizontal plane and where z is the vertical coordinate. In the limit of a small gap, the thickness profile of the fluid between the sphere and the undeformed fluid interface can be approximated by its parabolic expansion, leading to

$$h(r,t) \simeq d(t) + \frac{r^2}{2a}. \tag{2.3}$$

The no-slip boundary condition is imposed at both the sphere's surface and the fluid interface. Hence, in the frame of the moving sphere, at $z = h$, one has

$$\boldsymbol{v} = \boldsymbol{0}, \tag{2.4}$$

and at the interface, i.e. $z = \delta$, one has

$$\boldsymbol{v} = -\boldsymbol{u} = -u\boldsymbol{e}_x. \tag{2.5}$$

Given the boundary conditions above, we can easily write the horizontal velocity profile in the gap between the sphere and the interface as

$$\boldsymbol{v} = \frac{\boldsymbol{\nabla} p}{2\eta}(z-h)(z-\delta) + \boldsymbol{u}\frac{z-h}{h-\delta}. \tag{2.6}$$

The conservation of the fluid volume in the gap allows for the derivation of the Reynolds thin-film equation for the system, which reads

$$\frac{\partial}{\partial t}(h-\delta) = \boldsymbol{\nabla}\cdot\left[\frac{\boldsymbol{\nabla} p}{12\eta}(h-\delta)^3 + \frac{\boldsymbol{u}}{2}(h-\delta)\right]. \tag{2.7}$$

The deflection of the fluid interface is controlled by the Laplace pressure jump. Thus, at $z = \delta$, one has

$$p \simeq \sigma\nabla^2\delta + g\delta(\rho - \rho_{sl}), \tag{2.8}$$

where we have assumed a small deformation of the interface and linearized the curvature.

Let us now non-dimensionalize the equations through

$$\left.\begin{aligned} d(t) = d^* D(T), \quad h(r,t) = d^* H(R,T), \quad \boldsymbol{r} = l\boldsymbol{R}, \quad z = d^* Z, \\ t = \frac{l}{c}T, \quad \boldsymbol{v}(\boldsymbol{r},z,t) = cV(\boldsymbol{R},Z,T), \quad \boldsymbol{u}(t) = cU(T)\boldsymbol{e}_x, \\ p(\boldsymbol{r},t) = \frac{\eta c l}{d^{*2}}P(\boldsymbol{R},T), \quad \delta(\boldsymbol{r},t) = d^*\Delta(\boldsymbol{R},T), \end{aligned}\right\} \tag{2.9}$$

where c and d^* represent characteristic in-plane velocity and gap-thickness scales, respectively, with $l = \sqrt{2ad^*}$ denoting the characteristic hydrodynamic radius.

At this point, we discuss the assumption of an infinitely viscous bottom layer and the resulting vanishing of the velocity, which has been previously addressed in the literature (Yiantsios & Davis 1990). Since the bottom fluid layer is considered to be much thicker than the upper one, the flow generated in the former evolves over a much larger length scale, typically given by a. As a consequence, by adapting the thin-bilayer-film normal stress balance (see (A4) in Bertin *et al.* 2021) to the current case of a thick bottom layer, we find that the dimensionless normal viscous stress at the fluid interface has a $(\eta_{sl}/\eta)(d^*/l)^4$ prefactor. We assume this numerical prefactor to be very small in our study, due to the vanishing of d^*/l, despite the large viscosity ratio – thus the non-inclusion of bottom-layer stress terms in (2.8).

In dimensionless terms, the undeformed thickness profile and Reynolds equation become

$$H(R, T) \simeq D(T) + R^2, \tag{2.10}$$

and

$$\frac{\partial}{\partial T}(H - \Delta) = \boldsymbol{\nabla} \cdot \left[\frac{\boldsymbol{\nabla} P}{12}(H - \Delta)^3 + \frac{\boldsymbol{U}}{2}(H - \Delta) \right]. \tag{2.11}$$

Besides, the deflection field Δ is related to the excess pressure field P by the dimensionless version of the Laplace equation, which reads

$$\nabla^2 \Delta - Bo\Delta = \kappa P, \tag{2.12}$$

where $Bo = (l/l_c)^2$ denotes the Bond number, $l_c = \sqrt{\sigma/[g(\rho_{sl} - \rho)]}$ denotes the capillary length and where we have introduced the capillary compliance of the interface, denoted by

$$\kappa = \frac{\eta c l^3}{\sigma d^{*3}}. \tag{2.13}$$

3. Perturbation analysis

As in previous studies regarding soft lubrication (Sekimoto & Leibler 1993; Skotheim & Mahadevan 2005; Urzay *et al.* 2007; Snoeijer *et al.* 2013; Salez & Mahadevan 2015; Essink *et al.* 2021; Bertin *et al.* 2022), we perform an asymptotic expansion of the unknown fields at first order in dimensionless capillary compliance, κ, as

$$\Delta \simeq \kappa \Delta_1 + O(\kappa^2), \tag{3.1}$$

$$P \simeq P_0 + \kappa P_1 + O(\kappa^2), \tag{3.2}$$

where $\kappa^i \Delta_i$ is the ith-order contribution to the deflection of the interface, and $\kappa^i P_i$ is the ith-order contribution to the excess pressure field.

3.1. *Zeroth-order pressure*

At zeroth order in κ, (2.11) reduces to

$$\dot{D} = \boldsymbol{\nabla} \cdot \left(\frac{\boldsymbol{\nabla} P_0}{12} H^3 + \boldsymbol{U} \frac{H}{2} \right). \tag{3.3}$$

This equation is identical to the one for a perfectly rigid, flat and no-slip boundary. Since the zeroth-order pressure field results from linear terms in velocity, we decompose it azimuthally as

$$P_0(\boldsymbol{R}, T) = P_{00}(R, T) + P_{01}(R, T) \cos\theta, \tag{3.4}$$

with R and θ the horizontal polar coordinates of $\boldsymbol{R}$. Assuming a vanishing pressure field at large R, and that it must remain finite and single valued at $R = 0$, the equations can be solved to give the zeroth-order components of the excess pressure field as (O'Neill & Stewartson 1967)

$$P_{00} = -\frac{3\dot{D}}{2(D + R^2)^2}, \tag{3.5}$$

$$P_{01} = \frac{6UR}{5(D + R^2)^2}. \tag{3.6}$$

3.2. *Interface deflection*

We now decompose the first-order deflection of the interface azimuthally as

$$\Delta_1(\boldsymbol{R}, T) = \Delta_{10}(R, T) + \Delta_{11}(R, T)\cos\theta. \tag{3.7}$$

Writing (2.12) at first order in κ, one has

$$\frac{1}{R}\frac{\partial}{\partial R}\left(R\frac{\partial \Delta_{10}}{\partial R}\right) - Bo\Delta_{10} = P_{00}, \tag{3.8}$$

and

$$\frac{1}{R}\frac{\partial}{\partial R}\left(R\frac{\partial \Delta_{11}}{\partial R}\right) - \frac{\Delta_{11}}{R^2} - Bo\Delta_{11} = P_{01}, \tag{3.9}$$

with the boundary conditions $\Delta_{1i} \to 0$ as $R \to \infty$, and finite and single-valued Δ_{1i} at $R = 0$. The solutions of the above equations can be written in the most general form as

$$\begin{aligned}\Delta_{10}(R) = &-I_0(\sqrt{Bo}R)\int_R^\infty K_0(\sqrt{Bo}\xi)\xi P_{00}(\xi)\,\mathrm{d}\xi \\ &- K_0(\sqrt{Bo}R)\int_0^R I_0(\sqrt{Bo}\xi)\xi P_{00}(\xi)\,\mathrm{d}\xi,\end{aligned} \tag{3.10}$$

$$\begin{aligned}\Delta_{11}(R) = &-I_1(\sqrt{Bo}R)\int_R^\infty K_1(\sqrt{Bo}\xi)\xi P_{01}(\xi)\,\mathrm{d}\xi \\ &- K_1(\sqrt{Bo}R)\int_0^R I_1(\sqrt{Bo}\xi)\xi P_{01}(\xi)\,\mathrm{d}\xi,\end{aligned} \tag{3.11}$$

where I_j and K_j denote the jth-order modified Bessel functions of the first and second kinds, respectively.

To understand the parametric influence of the Bond number Bo, we explore the behaviours of the interface deflection for both small and large Bo values. For vanishing Bo, the anisotropic deflection component Δ_{11} reaches a limiting behaviour given by the following expression:

$$\Delta_{11} \simeq -\frac{3U}{10}\frac{\ln\left(1 + \dfrac{R^2}{D}\right)}{R}. \tag{3.12}$$

In contrast, the isotropic deflection component Δ_{10} does not show any limiting behaviour at vanishing Bo, and a reduction in Bo leads to an unbounded increase in Δ_{10}. To understand the behaviour of Δ_{10} as $Bo \to 0$, we take an asymptotic approach previously used in problems relating to capillary deformations (James 1974; Lo 1983; Dupré de Baubigny *et al.* 2015). The vanishing of Bo allows for a scale separation in the radial coordinate R into: (i) an inner region controlled by surface tension; and (ii) an outer region, where gravity is present. In the inner region ($R \ll 1/\sqrt{Bo}$), the interface deformation

denoted by Δ_{10}^{i} satisfies

$$\frac{1}{R}\frac{\partial}{\partial R}\left(R\frac{\partial \Delta_{10}^{i}}{\partial R}\right) = P_{00}. \tag{3.13}$$

The general solution of the above equation reads

$$\Delta_{10}^{i} = \mathcal{A} - \frac{3\dot{D}}{8D}\ln(D + R^2), \tag{3.14}$$

where $\mathcal{A}$ is an integration constant. The far-field behaviour of the inner solution reads

$$\Delta_{10}^{i} \sim \mathcal{A} - \frac{3\dot{D}}{4D}\ln(R). \tag{3.15}$$

In the outer region ($R \gg 1/\sqrt{Bo}$), gravity matters but there is no lubrication pressure, which leads to the following governing equation for the interface deformation denoted by Δ_{10}^{o}:

$$\frac{1}{R}\frac{\partial}{\partial R}\left(R\frac{\partial \Delta_{10}^{o}}{\partial R}\right) - Bo\,\Delta_{10}^{o} = 0. \tag{3.16}$$

The latter equation is solved, along with the condition that the deflection vanishes at infinity, leading to

$$\Delta_{10}^{o} = \mathcal{B}K_0(\sqrt{Bo}R), \tag{3.17}$$

where $\mathcal{B}$ is an integration constant. The near-field behaviour of the outer solution reads

$$\Delta_{10}^{o} \sim -\mathcal{B}\left(\gamma - \ln 2 + \frac{\ln Bo}{2} + \ln R\right), \tag{3.18}$$

where γ is Euler's constant. Matching (3.15) with (3.18) leads to

$$\mathcal{A} = -\frac{3\dot{D}}{4D}\left(\gamma - \ln 2 + \frac{\ln Bo}{2}\right), \tag{3.19}$$

$$\mathcal{B} = \frac{3\dot{D}}{4D}. \tag{3.20}$$

Substituting these constants in (3.14) and (3.17), we find the matched asymptotes of the interface deflection at small Bo. The interface deflection can then be approximated by the matched cross-over expression

$$\Delta_{10}|_{Bo\to 0} \approx \frac{3\dot{D}}{4D}\left[K_0(\sqrt{Bo}R) + \frac{1}{2}\ln\left(\frac{R^2}{D + R^2}\right)\right]. \tag{3.21}$$

The interface deflection is shown in figure 2 at a fixed low value of Bo. The cross-over expression at small Bo described above matches the exact one calculated using (3.10), with improving precision as Bo reduces. Figure 2 also shows the inner and outer solutions, which diverge in the far and near fields, respectively.

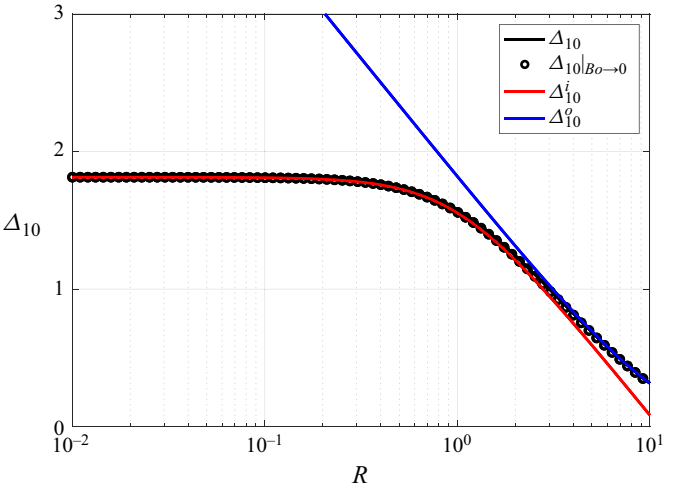

Figure 2. Isotropic component Δ_{10} of the amplitude of the first-order interface deflection as a function of the radial coordinate R (solid black line), as calculated from (3.10), for $Bo = 0.01$, $D = 1$ and $\dot{D} = 1$. For comparison, the inner solution (red solid line), the outer solution (blue solid line) and the matched cross-over expression (symbols), from (3.14), (3.17) and (3.21), respectively, are also shown.

The other interesting limit arises when $Bo \to \infty$, leading to the curvature-related terms in (3.8)–(3.9) dropping out, giving us

$$\Delta_{10} = -\frac{P_{00}}{Bo} = \frac{3\dot{D}}{2Bo(D+R^2)^2}, \tag{3.22}$$

$$\Delta_{11} = -\frac{P_{01}}{Bo} = -\frac{6UR}{5Bo(D+R^2)^2}. \tag{3.23}$$

As a consequence, the deflection is directly proportional to the pressure applied, with $\kappa/Bo = \eta cl/[gd^{*3}(\rho_{sl} - \rho)]$ as an effective compliance. From the latter, we see that in the limit of large Bo the surface tension no longer controls the deformation. This large-Bo response is akin to the Winkler response for thin compressible elastic materials, which has been studied previously (Skotheim & Mahadevan 2005; Urzay *et al.* 2007; Salez & Mahadevan 2015; Chandler & Vella 2020; Bertin *et al.* 2022).

Apart from these two extremes, further exploration of the influence of Bo can be done using (3.10) and (3.11). Figure 3 shows the isotropic and anisotropic profiles of the amplitude of the first-order interface deflection, for different values of Bo. We see that capillarity leads to a long-ranged interface deflection whose range and magnitude both decrease with increasing Bo.

3.3. *First-order pressure*

At first order in κ, the pressure field involves in particular the squared velocity, and can thus be decomposed as

$$P_1(\boldsymbol{R}, T, Bo, D) = P_{10}(R, T, Bo, D) + P_{11}(R, T, Bo, D)\cos\theta + P_{12}(R, T, Bo, D)\cos 2\theta. \tag{3.24}$$

The governing equations for the components P_{1i} of the first-order magnitude P_1 of the excess pressure field can be derived by considering (2.11) at first order in κ. Since P_{12} is

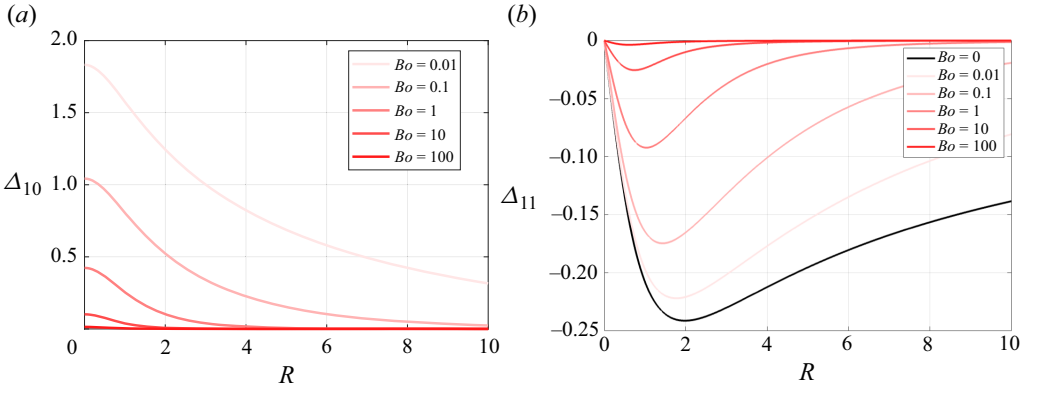

Figure 3. Isotropic component Δ_{10} (*a*) and anisotropic component Δ_{11} (*b*) of the amplitude of the first-order interface deflection as a function of the radial coordinate R, as calculated from (3.10) and (3.11), for $D = 1$, various Bo as indicated, and for either $\dot{D} = 1$ (*a*) or $U = 1$ (*b*). The black solid line denotes the limiting profile for $Bo = 0$ in the anisotropic case, as given in (3.12).

not needed to compute the forces and torques, we restrict ourselves to the two following equations:

$$\frac{1}{R}\frac{\partial}{\partial R}\left(RH^3\frac{\partial P_{10}}{\partial R}\right) = \frac{1}{R}\frac{\partial}{\partial R}\left[3RH^2\left(\Delta_{10}\frac{\partial P_{00}}{\partial R} + \frac{\Delta_{11}}{2}\frac{\partial P_{01}}{\partial R}\right)\right] + 3U\frac{\partial \Delta_{11}}{\partial R} + 3U\frac{\Delta_{11}}{R} - 12\frac{\partial \Delta_{10}}{\partial T}, \tag{3.25}$$

$$\frac{1}{R}\frac{\partial}{\partial R}\left(RH^3\frac{\partial P_{11}}{\partial R}\right) - \frac{H^3}{R^2}P_{11} = \frac{1}{R}\frac{\partial}{\partial R}\left[3RH^2\left(\Delta_{10}\frac{\partial P_{01}}{\partial R} + \Delta_{11}\frac{\partial P_{00}}{\partial R}\right)\right] - \frac{3H^2\Delta_{10}P_{01}}{R^2} + 6U\frac{\partial \Delta_{10}}{\partial R} - 12\frac{\partial \Delta_{11}}{\partial T}. \tag{3.26}$$

Using the linearity of the equations above, the components of the pressure field can be expressed as follows:

$$P_{10} = \frac{U^2}{D^2}\phi_{U^2} + \frac{\dot{D}^2}{D^3}\phi_{\dot{D}^2} + \frac{\ddot{D}}{D^2}\phi_{\ddot{D}}, \tag{3.27}$$

$$P_{11} = \frac{\dot{U}}{D}\phi_{\dot{U}} + \frac{U\dot{D}}{D^2}\phi_{U\dot{D}}, \tag{3.28}$$

where the ϕ_k represent the auxiliary functions for the corresponding second-order forcing parameters k, such as U^2 etc., which all vary with distance R and depend upon the values of D and Bo. These functions can then be evaluated by numerically solving (3.25)–(3.26), together with the boundary conditions that the pressure vanishes in the far field and remains finite and single valued at the origin. The results are shown in figures 4 and 5. For all components, as Bo increases, the magnitudes of the auxiliary functions decrease due to the decreasing interface deflection. Interestingly, even though the deflection studied above is long ranged, the pressure field decays quite rapidly.

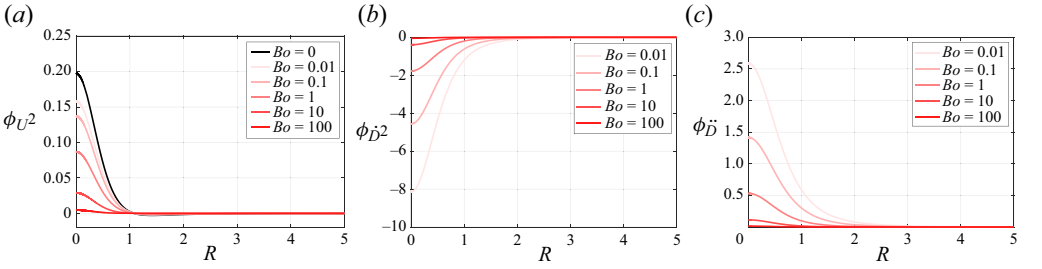

Figure 4. Auxiliary functions ϕ_k (see (3.27)) of the isotropic component P_{10} of the first-order magnitude P_1 of the excess pressure field, as functions of the radial coordinate R, for various Bond numbers Bo, as obtained by numerically solving (3.25) with $D = 1$.

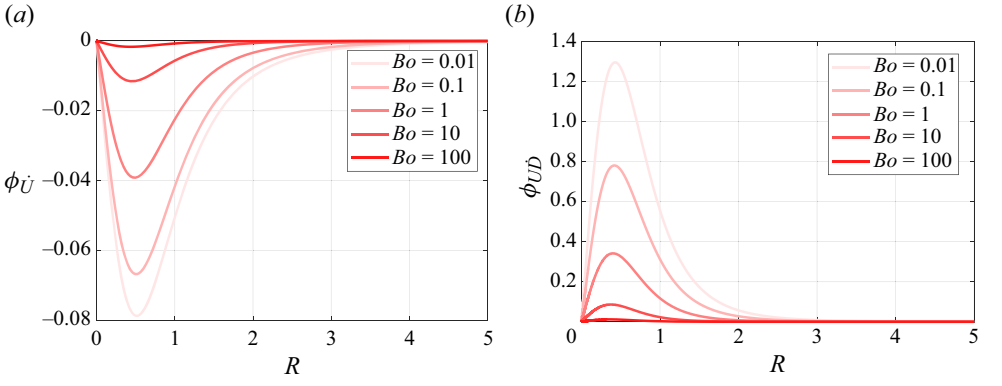

Figure 5. Auxiliary functions ϕ_k (see (3.28)) of the anisotropic component P_{11} of the first-order magnitude P_1 of the excess pressure field, as functions of the radial coordinate R, for various Bond numbers Bo, as obtained by numerically solving (3.26) with $D = 1$.

4. Capillary-lubrication forces and torques

Since the zeroth-order forces and torques acting on the sphere are identical to the known ones for the motion near a rigid, flat and no-slip boundary, we focus here on the first-order forces and torques acting on the sphere, and resulting from the interface deflection. These can be calculated from the stress tensor $\boldsymbol{\Sigma}$, that reads in the lubrication approximation: $\boldsymbol{\Sigma} \simeq -p\boldsymbol{I} + \eta \boldsymbol{e}_z \partial_z \boldsymbol{v}$, where $\boldsymbol{I}$ denotes the identity tensor. In dimensional units, the first-order vertical force acting on the sphere can be evaluated as

$$f_{z,1} \simeq \frac{2^{5/2}\pi\kappa\eta c a^{3/2}}{d^{*1/2}} \int_0^\infty P_{10}(R) R \, \mathrm{d}R, \tag{4.1}$$

which can be decomposed using the auxiliary functions calculated before as

$$f_{z,1} \simeq \alpha_{U^2} \frac{\eta^2 u^2 a^3}{\sigma d^2} - \alpha_{\dot{D}^2} \frac{\eta^2 \dot{d}^2 a^4}{\sigma d^3} + \alpha_{\ddot{D}} \frac{\eta^2 \ddot{d} a^4}{\sigma d^3}, \tag{4.2}$$

where the α_k (with k indicating here the forcing source, such as U^2) are the prefactors of the respective scalings. These prefactors are plotted in figure 6 as functions of Bo. An important difference arises between the various prefactors at small Bo. Indeed the prefactor α_{U^2} reaches a plateau, whereas $\alpha_{\ddot{D}}$ and $\alpha_{\dot{D}^2}$ increase logarithmically with decreasing Bo. These asymptotic behaviours at small Bo can be calculated using the

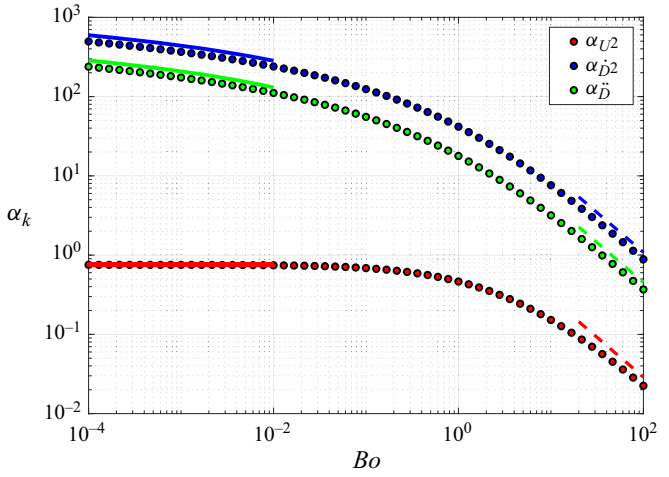

Figure 6. Prefactors α_k of the scalings of the vertical-force terms, defined in (4.2), as functions of Bond number Bo. The solid and dashed lines correspond to the small- and large-Bo behaviours (see table 1), respectively.

α_k, β_k	$Bo \to 0$	$Bo \to \infty$
α_{U^2}	$6\pi/25$	$96\pi/(125Bo)$
$\alpha_{\dot{D}^2}$	$-6\pi[2 + 6\gamma + 3\ln(Bo/4)]$	$144\pi/(5Bo)$
$\alpha_{\ddot{D}}$	$-9\pi[1 + 2\gamma + \ln(Bo/4)]$	$12\pi/Bo$
$\beta_{U\dot{D}}$	$-24\pi[4 + 10\gamma + 5\ln(Bo/4)]/25$	$968\pi/(125Bo)$
$\beta_{\dot{U}}$	$36\pi/25$	$24\pi/(25Bo)$

Table 1. Asymptotic behaviours of the scaling prefactors α_k and β_k at small (see Appendix A) and large (see Bertin *et al.* 2022) Bond numbers Bo, where γ denotes Euler's constant.

Lorentz reciprocal theorem (Daddi-Moussa-Ider *et al.* 2018; Rallabandi *et al.* 2018; Masoud & Stone 2019), by invoking as well (3.12) and (3.21), as detailed in Appendix A and summarized in table 1. They are in agreement with the numerical solutions, as shown in figure 6. Besides, as Bo increases, all the prefactors decrease, and this decrease becomes inversely proportional to Bo in the large-Bo limit, highlighting the transition to the Winkler-like regime. The corresponding asymptotic expressions have been calculated previously (Bertin *et al.* 2022), are summarized in table 1, and are in agreement with the numerical solutions, as shown in figure 6.

Similarly, the horizontal force acting on the sphere is given by the expression (Bertin *et al.* 2022)

$$f_{x,1} \simeq 2\pi\eta ca\kappa \int_0^\infty \left[-2RP_{11} - \frac{H}{2}\left(\partial_R P_{11} + \frac{P_{11}}{R}\right) + \frac{\Delta_{11}}{2}\partial_R P_{00} + \frac{\Delta_{10}}{2}\left(\partial_R P_{01} + \frac{P_{01}}{R}\right) - 2\frac{U\Delta_{10}}{H^2}\right] R\,\mathrm{d}R, \tag{4.3}$$

which can be decomposed into

$$f_{x,1} \simeq -\beta_{U\dot{D}}\frac{\eta^2 u\dot{d}a^3}{\sigma d^2} + \beta_{\dot{U}}\frac{\eta^2 \dot{u}a^3}{\sigma d}, \tag{4.4}$$

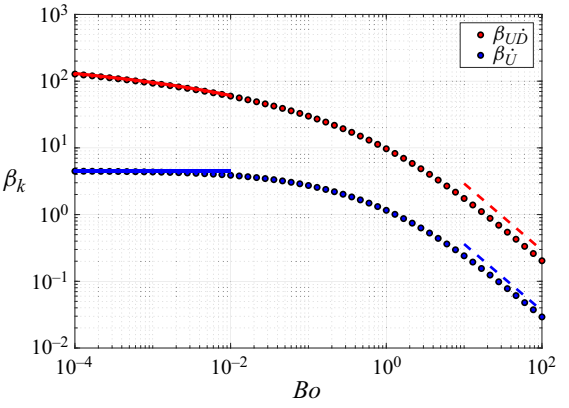

Figure 7. Prefactors β_k of the scalings of the horizontal-force terms, defined in (4.4), as functions of Bond number Bo. The solid and dashed lines correspond to the small- and large-Bo behaviours (see table 1), respectively.

where the β_k (with k indicating here the forcing source, such as $\dot{U}$) are the prefactors of the respective scalings. These prefactors are plotted in figure 7 as functions of Bo. An important difference arises once again between the two prefactors at small Bo. Indeed, the prefactor $\beta_{\dot{U}}$ reaches a plateau, whereas $\beta_{U\dot{D}}$ increases logarithmically with decreasing Bo. These asymptotic behaviours at small Bo can be once again calculated using the Lorentz reciprocal theorem, as detailed in Appendix A and summarized in table 1. They are in agreement with the numerical solutions, as shown in figure 7. Besides, as Bo increases, all the prefactors decrease, and this decrease becomes inversely proportional to Bo in the large-Bo limit, highlighting once again the transition to the Winkler-like regime. The corresponding asymptotic expressions have been calculated previously (Bertin *et al.* 2022), are summarized in table 1 and are in agreement with the numerical solutions, as shown in figure 7.

As shown in previous studies (Salez & Mahadevan 2015; Bertin *et al.* 2022), the contributions to the first-order torque felt by the sphere along the y-axis have the same numerical prefactors as those for the first-order horizontal force, with the inclusion of a supplementary length-scale factor a. Hence, the first-order torque exerted on the sphere is given by

$$\tau_{y,1} \simeq \beta_{U\dot{D}} \frac{\eta^2 u \dot{d} a^4}{\sigma d^2} - \beta_{\dot{U}} \frac{\eta^2 \dot{u} a^4}{\sigma d}. \tag{4.5}$$

We conclude this whole section with an important remark. The cross-over from the capillary-dominated to the Winkler-like regime occurs at $Bo \sim 1$. This occurs when the hydrodynamic radius is comparable to the capillary length. Since typical capillary lengths are of the order of $\sim$1 mm, and given the lubrication conditions, such a cross-over can only be felt with spheres of millimetric radii and above.

5. Conclusion

Using capillary-lubrication theory, scaling arguments and numerical integrations, we explored the asymptotic forces and torques generated on a sphere in translational motion within a viscous fluid, in close proximity to a deformable capillary interface with another, infinitely viscous fluid on the other side. Due to a symmetry between translational

and rotational motions in soft lubrication (Bertin *et al.* 2022), our work immediately generalizes to the case where rotation would be added. Specifically, by employing a perturbation analysis in the limit of small deformation of the fluid interface, we calculated the pressure fields decomposed into their various contributions from different degrees of freedom of the sphere. We investigated in particular the effects of gravity, which not only change the scaling laws of the forces and torques, but also show a Winkler-like elastic response at large Bond numbers. Altogether, our results allow us to quantify and possibly control soft-lubricated motion near tensile interfaces, which are ubiquitous in soft matter and biological physics. For example, the visco-capillary lift force revealed among others by our analysis, could contribute to the rationalization of the swimming of active organisms at the air–water interface (Trouilloud *et al.* 2008), the self-propulsion of levitating Leidenfrost droplets (Gauthier *et al.* 2019) for which a detailed mechanism is lacking to date or the thermal motion of oil droplets near rigid walls for which intriguing transient non-conservative forces have been reported (Fares *et al.* 2024).

Acknowledgements. The authors thank G. Audéoud, V. Bertin and I. Cantat for interesting discussions.

Funding. The authors acknowledge financial support from the European Union through the European Research Council under EMetBrown (ERC-CoG-101039103) grant. Views and opinions expressed are, however, those of the authors only and do not necessarily reflect those of the European Union or the European Research Council. Neither the European Union nor the granting authority can be held responsible for them. The authors also acknowledge financial support from the Agence Nationale de la Recherche under Softer (ANR-21-CE06-0029) and Fricolas (ANR-21-CE06-0039) grants. Finally, they thank the Soft Matter Collaborative Research Unit, Frontier Research Center for Advanced Material and Life Science, Faculty of Advanced Life Science at Hokkaido University, Sapporo, Japan.

Declaration of interests. The authors report no conflict of interest.

Author ORCIDs.
Aditya Jha https://orcid.org/0000-0002-9520-7578;
Thomas Salez https://orcid.org/0000-0001-6111-8721.

Appendix A. Lorentz reciprocal theorem

In this appendix, we employ the Lorentz reciprocal theorem for Stokes flows (Daddi-Moussa-Ider *et al.* 2018; Rallabandi *et al.* 2018; Masoud & Stone 2019) in the limit of vanishing Bond number Bo, which allows us to evaluate the asymptotic behaviours of the scaling prefactors α_k and β_k.

A.1. *Vertical force*

The model problem introduced to perform the calculation comprises a sphere moving in a viscous fluid and towards an immobile, rigid, planar surface. We denote by $\hat{\boldsymbol{V}}_\perp = -\hat{V}_\perp \boldsymbol{e}_z$ the velocity at the particle's surface while assuming a no-slip boundary condition at the wall's surface located at $z = 0$. The model problem is described by the incompressible Stokes equations, $\boldsymbol{\nabla} \cdot \hat{\boldsymbol{\Sigma}} = 0$ and $\boldsymbol{\nabla} \cdot \hat{\boldsymbol{v}}_\perp = 0$, where $\hat{\boldsymbol{\Sigma}}$ denotes the stress tensor of the model problem and $\boldsymbol{v}_\perp$ denotes the corresponding fluid velocity. We invoke lubrication theory to obtain the corresponding pressure and velocity fields, given by

$$\hat{p}_\perp(\boldsymbol{r}) = \frac{3\eta \hat{V}_\perp a}{\hat{h}^2(r)}, \tag{A1}$$

$$\hat{\boldsymbol{v}}_\perp(\boldsymbol{r}, z) = \frac{\boldsymbol{\nabla}\hat{p}_\perp(\boldsymbol{r})}{2\eta} z[z - \hat{h}(r)], \tag{A2}$$

where

$$\hat{h}(r) \simeq d + \frac{r^2}{2a}. \tag{A3}$$

From the Lorentz reciprocal theorem, one has

$$\int_{\mathcal{S}} \boldsymbol{n} \cdot \boldsymbol{\Sigma} \cdot \hat{\boldsymbol{v}}_\perp \, \mathrm{d}s = \int_{\mathcal{S}} \boldsymbol{n} \cdot \hat{\boldsymbol{\Sigma}} \cdot \boldsymbol{v} \, \mathrm{d}s, \tag{A4}$$

where $\boldsymbol{\Sigma}$ and $\boldsymbol{v}$ denote the stress tensor and flow velocity for the real problem, with $\mathcal{S}$ denoting the entire bounding surface, including the surface of the sphere, the surface of the substrate and the surface located at $\boldsymbol{r} \to \infty$. The unit vector normal to the surface pointing towards the fluid is denoted by $\boldsymbol{n}$. Given the boundary conditions of the model problem, the above relation simplifies to give

$$F_z = -\frac{1}{\hat{V}_\perp} \int_{\mathcal{S}} \boldsymbol{n} \cdot \hat{\boldsymbol{\Sigma}} \cdot \boldsymbol{v} \, \mathrm{d}s. \tag{A5}$$

To approximate the velocity field at the wall's surface, we perform a Taylor expansion accounting for the small deformation of the wall as

$$\boldsymbol{v}|_{z=0} \simeq \boldsymbol{v}|_{z=\delta} - \delta \partial_z \boldsymbol{v}_0|_{z=0}, \tag{A6}$$

$$= -u\boldsymbol{e}_x - \dot{d}\boldsymbol{e}_z + (\partial_t - u\partial_x)\delta \boldsymbol{e}_z - \delta \partial_z \boldsymbol{v}_0|_{z=0}, \tag{A7}$$

where $\boldsymbol{v}_0$ denotes the zeroth-order velocity field corresponding to a sphere moving near a rigid surface. Thus, the leading-order normal force simplifies to

$$F_{z,1} \simeq -\frac{1}{\hat{V}_\perp} \int_{\mathbb{R}^2} (\hat{p}_\perp(\partial_t - u\partial_x)\delta + \eta \partial_z \hat{\boldsymbol{v}}_\perp|_{z=0} \cdot \partial_z \boldsymbol{v}_0|_{z=0}) \, \mathrm{d}\boldsymbol{r}. \tag{A8}$$

Computing the latter integral by considering the deflection δ (or Δ in dimensionless variables) generated at vanishing *Bo* allows us to recover the asymptotic expressions presented in table 1.

A.2. *Horizontal force*

The model problem consists here of a sphere translating with a velocity $\hat{V}_\parallel \boldsymbol{e}_x$, parallel to and near an immobile and rigid substrate with no-slip boundary conditions applied at both the surfaces of the sphere and the substrate. A similar treatment as in the previous section leads to

$$\hat{p}_\parallel(\boldsymbol{r}) = \frac{6\eta \hat{V}_\parallel r \cos\theta}{5\hat{h}^2(r)}, \tag{A9}$$

$$\hat{\boldsymbol{v}}_\parallel(\boldsymbol{r}, z) = \frac{\boldsymbol{\nabla}\hat{p}_\parallel(\boldsymbol{r})}{2\eta} z[z - \hat{h}(r)] + \hat{\boldsymbol{V}}_\parallel \frac{z}{\hat{h}(r)}, \tag{A10}$$

and

$$F_{x,1} \simeq -\frac{1}{\hat{V}_\parallel} \int_{\mathbb{R}^2} (\hat{p}_\parallel(\partial_t - u\partial_x)\delta + \eta \partial_z \hat{\boldsymbol{v}}_\parallel|_{z=0} \cdot \partial_z \boldsymbol{v}_0|_{z=0}) \, \mathrm{d}\boldsymbol{r}. \tag{A11}$$

Computing the latter integral by considering the deflection δ (or Δ in dimensionless variables) generated at vanishing *Bo* allows us to recover the asymptotic expressions presented in table 1.

References

Abkarian, M., Lartigue, C. & Viallat, A. 2002 Tank treading and unbinding of deformable vesicles in shear flow: determination of the lift force. *Phys. Rev. Lett.* **88**, 068103.

Aderogba, K. & Blake, J. 1978 Action of a force near the planar surface between two semi-infinite immiscible liquids at very low Reynolds numbers. *Bull. Austral. Math. Soc.* **18**, 345.

Balmforth, N.J., Cawthorn, C.J. & Craster, R.V. 2010 Contact in a viscous fluid. Part 2. A compressible fluid and an elastic solid. *J. Fluid Mech.* **646**, 339.

Basoli, F., Giannitelli, S.M., Gori, M., Mozetic, P., Bonfanti, A., Trombetta, M. & Rainer, A. 2018 Biomechanical characterization at the cell scale: present and prospects. *Frontiers Physiol.* **9**, 1449.

Batchelor, G. 1970 The stress system in a suspension of force-free particles. *J. Fluid Mech.* **41**, 545.

Batchelor, G. 1971 The stress generated in a non-dilute suspension of elongated particles by pure straining motion. *J. Fluid Mech.* **46**, 813.

Batchelor, G. 1976 Brownian diffusion of particles with hydrodynamic interaction. *J. Fluid Mech.* **74**, 1.

Batchelor, G. 1977 The effect of Brownian motion on the bulk stress in a suspension of spherical particles. *J. Fluid Mech.* **83**, 97.

Batchelor, G.K. 1967 *An Introduction to Fluid Dynamics*. Cambridge University Press.

Beaucourt, J., Biben, T. & Misbah, C. 2004 Optimal lift force on vesicles near a compressible substrate. *Europhys. Lett.* **67**, 676.

Bertin, V., Amarouchene, Y., Raphael, E. & Salez, T. 2022 Soft-lubrication interactions between a rigid sphere and an elastic wall. *J. Fluid Mech.* **933**, A23.

Bertin, V., Lee, C.L., Salez, T., Raphaël, E. & Dalnoki-Veress, K. 2021 Capillary levelling of immiscible bilayer films. *J. Fluid Mech.* **911**, A13.

Bouchet, A.-S., Cazeneuve, C., Baghdadli, N., Luengo, G.S. & Drummond, C. 2015 Experimental study and modeling of boundary lubricant polyelectrolyte films. *Macromolecules* **48**, 2244.

Bureau, L., Coupier, G. & Salez, T. 2023 Lift at low Reynolds number. *Eur. Phys. J.* E **46**, 111.

Chandler, T.G. & Vella, D. 2020 Validity of Winkler's mattress model for thin elastomeric layers: beyond Poisson's ratio. *Proc. R. Soc.* A **476**, 20200551.

Clarke, R. & Potnis, S. 2011 Elastohydrodynamics induced by a rapidly moving microscopic body. *Proc. R. Soc.* A **467**, 2852.

Collins, W. 1955 On the steady rotation of a sphere in a viscous fluid. *Mathematika* **2**, 42.

Cooley, M. & O'Neill, M. 1969 On the slow motion generated in a viscous fluid by the approach of a sphere to a plane wall or stationary sphere. *Mathematika* **16**, 37.

Daddi-Moussa-Ider, A., Rallabandi, B., Gekle, S. & Stone, H.A. 2018 Reciprocal theorem for the prediction of the normal force induced on a particle translating parallel to an elastic membrane. *Phys. Rev. Fluids* **3**, 084101.

Davies, H.S., Debarre, D., El Amri, N., Verdier, C., Richter, R.P. & Bureau, L. 2018 Elastohydrodynamic lift at a soft wall. *Phys. Rev. Lett.* **120**, 198001.

Dean, W. & O'Neill, M. 1963 A slow motion of viscous liquid caused by the rotation of a solid sphere. *Mathematika* **10**, 13.

Desai, N. & Ardekani, A.M. 2020 Biofilms at interfaces: microbial distribution in floating films. *Soft Matt.* **16**, 1731.

Dupré de Baubigny, J., Benzaquen, M., Fabié, L., Delmas, M., Aimé, J.-P., Legros, M. & Ondarçuhu, T. 2015 Shape and effective spring constant of liquid interfaces probed at the nanometer scale: finite size effects. *Langmuir* **31**, 9790.

Essink, M.H., Pandey, A., Karpitschka, S., Venner, C.H. & Snoeijer, J.H. 2021 Regimes of soft lubrication. *J. Fluid Mech.* **915**, A49.

Fares, N., Lavaud, M., Zhang, Z., Jha, A., Amarouchene, Y. & Salez, T. 2024 Observation of Brownian elastohydrodynamic forces acting on confined soft colloids. *Proc. Natl Acad. Sci. USA* **121**, e2411956121.

Garcia, L., Barraud, C., Picard, C., Giraud, J., Charlaix, E. & Cross, B. 2016 A micro-nano-rheometer for the mechanics of soft matter at interfaces. *Rev. Sci. Instrum.* **87**, 113906.

Gauthier, A., Diddens, C., Proville, R., Lohse, D. & van Der Meer, D. 2019 Self-propulsion of inverse Leidenfrost drops on a cryogenic bath. *Proc. Natl Acad. Sci. USA* **116**, 1174.

GELLER, A., LEE, S. & LEAL, L. 1986 The creeping motion of a spherical particle normal to a deformable interface. *J. Fluid Mech.* **169**, 27.

GOLDMAN, A.J., COX, R.G. & BRENNER, H. 1967 Slow viscous motion of a sphere parallel to a plane wall—I. Motion through a quiescent fluid. *Chem. Engng Sci.* **22**, 637.

HAPPEL, J. & BRENNER, H. 1983 *Low Reynolds Number Hydrodynamics: With Special Applications to Particulate Media*, vol. 1. Springer Science & Business Media.

HLAVÁČEK, M. 1993 The role of synovial fluid filtration by cartilage in lubrication of synovial joints – I. Mixture model of synovial fluid. *J. Biomech.* **26**, 1145.

HOU, J., MOW, V.C., LAI, W. & HOLMES, M. 1992 An analysis of the squeeze-film lubrication mechanism for articular cartilage. *J. Biomech.* **25**, 247.

HU, S., MENG, F. & DOI, M. 2023 Effect of fluid viscoelasticity, shear stress, and interface tension on the lift force in lubricated contacts. *J. Chem. Phys.* **159**, 164106.

JAMES, D.F. 1974 The meniscus on the outside of a small circular cylinder. *J. Fluid Mech.* **63**, 657.

JEFFREY, D. & ONISHI, Y. 1981 The slow motion of a cylinder next to a plane wall. *Q. J. Mech. Appl. Maths* **34**, 129.

JEFFERY, G. 1915 On the steady rotation of a solid of revolution in a viscous fluid. *Proc. Lond. Math. Soc.* **2**, 327.

JHA, A., AMAROUCHENE, Y. & SALEZ, T. 2023 Capillary-lubrication force exerted on a two-dimensional particle moving towards a thin fluid film. *J. Fluid Mech.* **977**, A50.

JHA, A., AMAROUCHENE, Y. & SALEZ, T. 2024 Capillary-lubrication force between rotating cylinders separated by a fluid interface. *Phys. Rev. Fluids* **9**, 074001.

KARGAR-ESTAHBANATI, A. & RALLABANDI, B. 2021 Lift forces on three-dimensional elastic and viscoelastic lubricated contacts. *Phys. Rev. Fluids* **6**, 034003.

LAMB, H. 1924 *Hydrodynamics*. University Press.

LEE, S., CHADWICK, R. & LEAL, L.G. 1979 Motion of a sphere in the presence of a plane interface. Part 1. An approximate solution by generalization of the method of Lorentz. *J. Fluid Mech.* **93**, 705.

LEE, S. & LEAL, L. 1980 Motion of a sphere in the presence of a plane interface. Part 2. An exact solution in bipolar co-ordinates. *J. Fluid Mech.* **98**, 193.

LEE, S. & LEAL, L. 1982 The motion of a sphere in the presence of a deformable interface: II. A numerical study of the translation of a sphere normal to an interface. *J. Colloid Interface Sci.* **87**, 81.

LEROY, S. & CHARLAIX, E. 2011 Hydrodynamic interactions for the measurement of thin film elastic properties. *J. Fluid Mech.* **674**, 389.

LEROY, S., STEINBERGER, A., COTTIN-BIZONNE, C., RESTAGNO, F., LÉGER, L. & CHARLAIX, E. 2012 Hydrodynamic interaction between a spherical particle and an elastic surface: a gentle probe for soft thin films. *Phys. Rev. Lett.* **108**, 264501.

LO, L.L. 1983 The meniscus on a needle–a lesson in matching. *J. Fluid Mech.* **132**, 65.

LOPEZ, D. & LAUGA, E. 2014 Dynamics of swimming bacteria at complex interfaces. *Phys. Fluids* **26**, 400.

MASOUD, H. & STONE, H.A. 2019 The reciprocal theorem in fluid dynamics and transport phenomena. *J. Fluid Mech.* **879**, P1.

NEZAMIPOUR, S. & NAJAFI, A. 2021 Flow pumping by external periodic shear applied to a soft interface. *Sci. Rep.* **11**, 15041.

O'NEILL, M. & STEWARTSON, K. 1967 On the slow motion of a sphere parallel to a nearby plane wall. *J. Fluid Mech.* **27**, 705.

O'NEILL, M.E. 1964 A slow motion of viscous liquid caused by a slowly moving solid sphere. *Mathematika* **11**, 67.

ORON, A., DAVIS, S. & BANKOFF, S. 1997 Long-scale evolution of thin liquid films. *Rev. Mod. Phys.* **69**, 931.

PANDEY, A., KARPITSCHKA, S., VENNER, C.H. & SNOEIJER, J.H. 2016 Lubrication of soft viscoelastic solids. *J. Fluid Mech.* **799**, 433–447.

RALLABANDI, B. 2024 Fluid-elastic interactions near contact at low Reynolds number. *Annu. Rev. Fluid Mech.* **56**, 491.

RALLABANDI, B., OPPENHEIMER, N., ZION, M.Y.B. & STONE, H.A. 2018 Membrane-induced hydroelastic migration of a particle surfing its own wave. *Nat. Phys.* **14**, 1211.

REYNOLDS, O. 1886 On the theory of lubrication and its application to Mr. Beauchamp tower's experiments, including an experimental determination of the viscosity of olive oil. *Phil. Trans. R. Soc. Lond.* **177**, 157.

RINEHART, A., LĀCIS, U., SALEZ, T. & BAGHERI, S. 2020 Lift induced by slip inhomogeneities in lubricated contacts. *Phys. Rev. Fluids* **5**, 082001.

SAINTYVES, B., JULES, T., SALEZ, T. & MAHADEVAN, L. 2016 Self-sustained lift and low friction via soft lubrication. *Proc. Natl Acad. Sci. USA* **113**, 5847.

SALEZ, T. & MAHADEVAN, L. 2015 Elastohydrodynamics of a sliding, spinning and sedimenting cylinder near a soft wall. *J. Fluid Mech.* **779**, 181.

SEKIMOTO, K. & LEIBLER, L. 1993 A mechanism for shear thickening of polymer-bearing surfaces: elasto-hydrodynamic coupling. *Europhys. Lett.* **23**, 113.

SKOTHEIM, J. & MAHADEVAN, L. 2005 Soft lubrication: the elastohydrodynamics of nonconforming and conforming contacts. *Phys. Fluids* **17**, 092101.

SNOEIJER, J.H., EGGERS, J. & VENNER, C.H. 2013 Similarity theory of lubricated hertzian contacts. *Phys. Fluids* **25**, 101705.

TROUILLOUD, R., YU, T.S., HOSOI, A. & LAUGA, E. 2008 Soft swimming: exploiting deformable interfaces for low Reynolds number locomotion. *Phys. Rev. Lett.* **101**, 048102.

URZAY, J., LLEWELLYN SMITH, S.G. & GLOVER, B.J. 2007 The elastohydrodynamic force on a sphere near a soft wall. *Phys. Fluids* **19**, 103106.

VIALAR, P., MERZEAU, P., GIASSON, S. & DRUMMOND, C. 2019 Compliant surfaces under shear: elastohydrodynamic lift force. *Langmuir* **35**, 15605.

WEEKLEY, S.J., WATERS, S.L. & JENSEN, O.E. 2006 Transient elastohydrodynamic drag on a particle moving near a deformable wall. *Q. J. Mech. Appl. Maths* **59**, 277.

YIANTSIOS, S.G. & DAVIS, R.H. 1990 On the buoyancy-driven motion of a drop towards a rigid surface or a deformable interface. *J. Fluid Mech.* **217**, 547.

ZHANG, Z., BERTIN, V., ARSHAD, M., RAPHAEL, E., SALEZ, T. & MAALI, A. 2020 Direct measurement of the elastohydrodynamic lift force at the nanoscale. *Phys. Rev. Lett.* **124**, 054502.